



Contents lists available at SciVerse ScienceDirect

Journal of Quantitative Spectroscopy & Radiative Transfer

journal homepage: www.elsevier.com/locate/jqsrt

Field measurement of clear-sky solar irradiance in Badain Jaran Desert of Northwestern China



Jianrong Bi^a, Jianping Huang^{a,*}, Qiang Fu^{a,b}, Jinming Ge^a, Jinsen Shi^a,
Tian Zhou^a, Wu Zhang^a

^a Key Laboratory for Semi-Arid Climate Change of the Ministry of Education and College of Atmospheric Sciences, Lanzhou University, Lanzhou 730000, PR China

^b Department of Atmospheric Sciences, University of Washington, Seattle, WA 98105, USA

ARTICLE INFO

Article history:

Received 12 June 2012
Received in revised form
23 July 2012
Accepted 24 July 2012
Available online 8 August 2012

Keywords:

Solar irradiance
Radiative closure experiment
Aerosol radiative forcing
Radiative heating rate

ABSTRACT

The Semi-Arid Climate and Environment Observatory of Lanzhou University (SACOL) sponsored and conducted an intensive field campaign on dust aerosols in Badain Jaran Desert of Northwestern China from April 20 to June 20, 2010. A set of state-of-the-art broadband radiometers and sun/sky photometers were deployed along with launched radiosonde. In this paper, we compared the simulated solar irradiances by using the SBDART radiative transfer model with those from the ground-based measurements for 69 selected cases of 7 days. It was shown that the averaged aerosol optical depth at 500 nm (AOD_{500}) is 0.18 ± 0.09 with AOD_{500} less than 0.5 for all cases. The single-scattering albedo and asymmetry factor at 675 nm are 0.928 ± 0.035 , 0.712 ± 0.023 , respectively. The AODs retrieved from the CIMEL sun photometer at various wavelengths agree well with those from the PREDE sky radiometer, and the columnar water vapor contents from CIMEL also agree well with radiosonde observations. In the radiative closure experiment, we used a collocated thermopile pyrgeometer with a shadow and ventilator to correct the thermal dome offset of diffuse irradiance measurement. The mean differences between model and measurements are -9.1 Wm^{-2} (-2.6%) for the direct irradiance, $+3.1 \text{ Wm}^{-2}$ ($+2.8\%$) for diffuse irradiance, and -6.0 Wm^{-2} (-1.3%) for global irradiance, which indicates an excellent radiative closure. Aerosol shortwave direct radiative forcing (ARF) and radiative heating rate are also investigated. The daily mean ARF ranges from -4.8 to $+0.4 \text{ Wm}^{-2}$ at the top of the atmosphere, -5.2 to -15.6 Wm^{-2} at the surface, and 5.2 to 10.8 Wm^{-2} in the atmosphere. The corresponding radiative heating rates for the whole atmosphere due to dust aerosols are 0.07, 0.11, 0.14, 0.11, 0.10, 0.08, and 0.07 K/day for the 7 selected cloudless days. These solar radiative forcing can be considered as the representative impact of background dust aerosol in Northwestern China.

© 2012 Elsevier Ltd. All rights reserved.

1. Introduction

Incident solar radiation is the primary energy source of the Earth–atmosphere system, which drives the formation and evolution of weather and climate processes.

When solar radiation passes through the atmosphere, the radiative energy budget is modulated by the absorption and scattering of air molecules, cloud droplets, and aerosol particles, and reflection of Earth's surface, which further modulate the thermal condition and atmospheric circulation [1–2]. A detailed and quantitative knowledge of radiative energy budget in both solar and terrestrial radiation is essential to accurately predict the Earth's climate and future climate change. A large number of

* Corresponding author. Fax: +86 931 891 4278.
E-mail address: hjp@lzu.edu.cn (J. Huang).

investigations have been done to simulate solar irradiances under clear sky conditions in the last few decades. Previous studies showed that radiative transfer models with observed input can accurately simulate the direct normal irradiances [3–6]. However, the diffuse irradiances from the radiative transfer models are usually higher than ground-based observations, with the maximum discrepancy of $\sim 30.0 \text{ Wm}^{-2}$ [4,7]. Henzing et al. [8] showed that model simulations may overestimate diffuse irradiances by about $7\text{--}44 \text{ Wm}^{-2}$ with an average value of 25 Wm^{-2} as compared with measurements. Kato et al. [4] suggested that an unknown gaseous absorber in the atmosphere could be responsible for the missing observed diffuse shortwave downward radiation (SDR) as compared with the models. Philipona [9] revealed that the “excessive” absorption can be partly interpreted by taking into account the thermal offsets of global and diffuse SDR measurements. However, a considerable difference in diffuse irradiances still appears even after considering the thermal offset corrections of pyranometer [10–11]. It is still an open question whether the discrepancy in solar diffuse radiances between model and observations is largely due to the error of model input parameters or ground-based measurements.

Recently, Halthore et al. [12] performed an intercomparison of 16 different radiative transfer models (RTM). They reported that for the aerosol-free and cloud-free conditions, all models agree to within 1% and 5%, respectively, in the dry and humid atmospheric conditions for the direct irradiances. And simulated diffuse surface irradiances are higher than measurements for all models using the same model inputs. These discrepancies could not be completely explained by instrumental uncertainty. Michalsky et al. [13] used six different radiative transfer models to simulate horizontal broadband shortwave irradiances at the Southern Great Plains during an aerosol intensive observation period (AIOP) of May 2003. They found that the biases between modeled and measured direct irradiances are in the worst case 1%, with less than 1.9% for diffuse irradiances. Their results are much better than previous radiative closure experiments due to better specification of input parameters and better measurements of irradiances. Wang et al. [14] also achieved an excellent clear-sky shortwave radiative closure at the

Cabauw Baseline Surface Radiation Network (BSRN) site in Netherlands through combination of Doubling Adding KNMI (DAK) model, Aerosol Robotic Network (AERONET) aerosol products and radiosonde data. They claimed that modeled solar irradiances can be improved by means of proper specification of DAK model input and high quality of the AERONET and BSRN measurements. However, Michalsky et al. [13] indicated that reducing the uncertainties of the inputs and irradiance measurements is an unfinished task, and further effort is warranted in testing more cases for very low aerosol optical depth days. Generally, accurate input parameters for the radiative transfer model and carefully calibrated shortwave spectral irradiance data are the key factors for simulations.

A comprehensive observational site was set up in Badain Jaran Desert of Northwestern China during the spring of 2010. The site comprises a CIMEL sun photometer, a PREDE sky radiometer and a suite of high precision broadband radiometers. These radiometers are newly purchased and calibrated by manufacturer immediately before installation (see Table 1). Before the deployment, the sun photometer and sky radiometer are also recently calibrated at the Mauna Loa Observatory (MLO; $19^{\circ}53' \text{ N}$, $155^{\circ}57' \text{ W}$, 3400 m above MSL) and Meteorological Research Institute (MRI; 36.056° N , $140.125^{\circ} \text{ E}$, 25 m above MSL) in Japan respectively. This provides us a great opportunity to compare the simulated and measured clear-sky solar irradiances in Northwestern China.

This paper is organized as follows. The observational site and instrumentation are described in Section 2. Section 3 depicts the ground-based radiation measurements and aerosol optical properties. Section 4 presents the comparison of model computations and ground-based measurements of solar irradiances. Aerosol direct radiative forcing and corresponding heating rate are drawn in the same section. Major conclusion and remarks are given in Section 5.

2. Site description and instrumentation

Semi-Arid Climate and Environment Observatory of Lanzhou University (SACOL) sponsored and conducted an intensive field experiment on dust aerosols from April 20 to June 20, 2010. One of primary scientific objectives of

Table 1

Key SMF instruments deployed for the field campaign at Minqin during spring of 2010.

Instrument	Manufacturer, model	Spectral range, measurement	Sensitivity ($\mu\text{V}/\text{W}/\text{m}^2$)
Pyranometer	Eppley, PSP ^a	0.285–2.8 μm , Global and diffuse radiation	Global: 8.46, diffuse: 8.48
	Eppley, B&W 8–48	0.285–2.8 μm , Global radiation	9.59
Pyheliometer	Eppley, NIP	0.285–2.8 μm , Direct radiation	8.38
	Kipp and Zonen, CHP1	0.7–3.0 μm , Direct radiation	7.73
Pyrgeometer	Eppley, PIR ^a	3.5–50 μm , Downward long wave radiation	Shadow: 2.98, without shadow: 2.76
UV radiometer	Eppley, TUVR	0.295–0.385 μm , Total UV radiation	174
Solar tracker	Kipp and Zonen, 2AP	0–360° azimuth, 0–90° elevation	Accuracy: $< 0.05^{\circ}$, repeat resolution: 0.0025°
Sun photometer	CIMEL Electro., CE-318	340, 380, 440, 500, 675, 870, 940, 1020 nm	AOD: 0.01–0.02
Sky radiometer	PREDE, POM-02	315, 340, 380, 400, 500, 675, 870, 940, 1020, 1600, 2200 nm	AOD: 0.01–0.02
Total sky imager	YES Inc., TSI880	352 × 288, 24-bit color JPEG format	Sampling rate: 1 min

^a is equipped with the Eppley ventilation system (VEN).

SACOL is to improve our understanding of the drought processes and associated climate change in Northwestern China [15]. SACOL's Mobile Facility (SMF) was deployed at Minqin (38.61°N, 102.96°E, 1373 m above MSL), a tiny isolated oasis surrounded by arid desert area in Northwestern China. The site lies in the middle of Hexi Corridor of Gansu province, adjacent to the southeast margin of Badain Jaran Desert and western border of Tenger Desert. Because of the nearby arid-desert regions, Minqin has extremely dry climate with a large amount of sunlight. The annual averaged precipitation there is merely 113.0 mm with approximately 60% of rainfall concentrates in summer, and evaporation is 2604 mm. The annual averaged temperature is 8.3 °C with huge annual and diurnal variations. The annual averaged wind speed is about 2.6 m/s, with high values appeared in spring. The unique geographical location and special land surface types combined with its dry climate and strong wind condition lead to frequent dust storms at Minqin during spring and early summer [16]. Therefore, Minqin has been established as one of permanent research sites for controlling desert advancement in Northwestern China.

2.1. Sun/sky radiometer measurements

A CIMEL sun photometer (Model CE-318) was set up at Minqin from May 18 to June 20, 2010. It is the standard instrument of the AERONET. The CIMEL sun/sky photometer makes measurements of the direct and diffuse sky radiances within the spectral range of 340–1020 nm. The automatic sun-tracking and sky scanning radiometer takes solar direct beam measurements with a 1.2° full field of view angle at every 15 min in eight spectral channels at 340, 380, 440, 500, 675, 870, 940, and 1020 nm (nominal wavelengths). Seven of the eight bands are used to acquire aerosol optical depth (AOD) data. The eighth band at 940 nm is used to retrieve total precipitable water content in centimeters. Holben et al. [17] and Eck et al. [18] reported that the total uncertainty in AOD for a field instrument is about 0.01–0.02. The details of water vapor path (WVP) retrieval procedure and errors involved can be found in Schmid et al. [19]. The retrieved precipitable water vapor path is congruent with radiosonde and microwave radiometer measurements within ~10%. Single scattering albedos (SSAs) are expected to have an uncertainty of 0.03–0.05 depending on aerosol type and loading [20]. Note that this uncertainty of SSAs is based on $AOD_{440} \geq 0.4$, and the uncertainty will become much larger when $AOD_{440} < 0.4$. The data sets used in this article come from the Level 1.5 quality-assured data of the AERONET (<http://aeronet.gsfc.nasa.gov>). They are pre- and post-field calibrated, automatically cloud screened [21]. Note that a spheroid particle shape assumption is used to simulate aerosol single scattering properties during dust periods.

In addition, a PREDE sky radiometer (Model POM-02) was deployed to observe simultaneously at Minqin. The PREDE sky radiometer is one of the key instruments which is widely used in the SKYNET—aerosol-cloud-radiation interaction ground-based observation network in East Asia [22]. A general description of the instrument's

configuration, data collection, calibration, and inversion algorithms were referred to Nakajima et al. [23]. It is mounted on a vertical–horizontal two-axis mount that is driven by digital servo motors to perform sky radiance almucantar measurements. And we can derive the aerosol optical properties (e.g., AOD, Ångström exponent, volume size distribution, SSA, ASY, and complex refractive index at 340, 380, 400, 500, 675, 870, and 1020 nm wavelengths) from its measurements as well.

2.2. Broadband solar radiation measurements

As mentioned above, Minqin is equipped with a large set of high precision broadband spectral instruments which can measure solar or shortwave radiation (SW) fluxes and terrestrial or longwave radiation (LW) fluxes (see Table 1). The quantities of solar direct and diffuse irradiances are measured independently by two normal incidence pyrheliometers (NIP, Eppley Lab. and CHP1, Kipp and Zonen) and a ventilated and shaded precision spectral pyranometer (PSP, Eppley) which were mounted on a two-axis automatic solar tracker (2AP, Kipp and Zonen) with tracking accuracy of 0.05°. A ventilated pyranometer (PSP) and another redundant black&white radiometer (B&W 8–48) without ventilator can measure directly global solar irradiance (0.285–2.85 μm). And the downward LW incoming radiations are measured with a ventilated and shaded pyrgeometer (PIR) and another ventilated PIR. The thermal offset of pyranometers during the daytime is corrected by considering the IR loss (see Section 3 for details). All radiation quantities are sampled at a 1-min time resolution and stored in a Campbell data logger. The quality assurance of data sets is carried out using the Baseline Surface Radiation Network (BSRN) quality control procedure, which includes: (i) physically possible limits test; (ii) extremely rare limits test; (iii) comparisons between the various radiation fluxes [24]. Furthermore, an inter-comparison of global irradiance measured by the two pyranometers and the global irradiance calculated as the sum of the solar direct NIP (or CHP1) and diffuse irradiance from PSP measurements can check and detect the abnormal data points.

2.3. Sky conditions measurements

A Total Sky Imager (Model TSI-880, YES Inc.) was set up to take continuously high-resolution pictures of the sky at a 1-minute interval during daytime. The model TSI-880 is an automatic, full-color, digital imaging sky camera with a software package that processes and analyzes the images to compute both cloud cover and sunshine duration, and stores the results. It captures images in JPEG format data files, which can be analyzed for fractional cloud cover. From the high-frequency snapshot images, a movie of the sky conditions is generated for each day. It has proven to be a very useful tool to assist in the separation of cloud scenes from dust events, or from clear sky scenes, as clouds are generally more variable than the atmospheric aerosols.

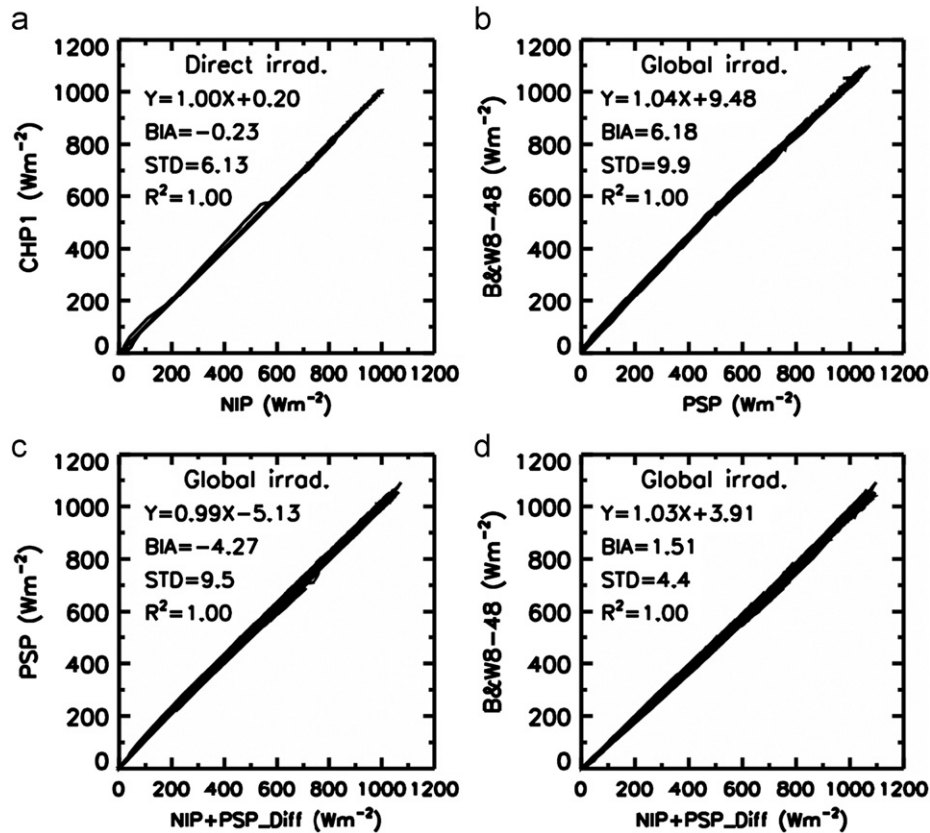


Fig. 1. Comparisons of ground-based solar irradiance measurements for (a) CHP1 versus NIP, (b) B&W 8–48 versus PSP, (c) PSP versus (NIP+PSP_Diffuse), and (d) B&W 8–48 versus (NIP+PSP_Diffuse).

3. Radiation data and model input parameters

3.1. Radiation data

Fig. 1 depicts an inter-comparison of various surface solar irradiances measured by different instruments. The results of inter-comparison are satisfactory. The correlation coefficients between the diverse quantities are highly significant, which are greater than or equal to 0.999 for all cases. We designate the bias error between the two variables as $BIA(=(Irr_y-Irr_x/Irr_x) \times 100\%)$. The discrepancies are -0.23% , 6.18% , -4.27% , and 1.51% for Fig. 1(a)–(d), respectively. From Fig. 1(a), we realize that direct normal irradiance measured from CHP1 agrees well with NIP. A difference value is equal to -0.84 Wm^{-2} between CHP1 and NIP measurements, which is much smaller than the prescribed accuracy of BSRN ($\sim 2 \text{ Wm}^{-2}$). The global irradiances from B&W 8–48 are about 35.3 and 10.7 Wm^{-2} larger than PSP and (NIP+PSP_Diff) respectively. Note that the thermal dome offset correction is only applied to PSP_Diff. It suggests that we have to correct the thermal dome offset for PSP global pyranometer. Additionally, B&W without ventilator can be to some extent accounted for this discrepancy. The differences between the PSP and (NIP+PSP_Diff), B&W 8–48 and (NIP+PSP_Diff) are partly ascribed to the cosine errors existing in PSP and B&W 8–48 pyranometers. Consequently, in order to avoid

these possible errors, we take advantage of global irradiance from (NIP+PSP_Diff) instead of horizontal broadband pyranometer in this paper.

Fig. 2 characterizes the daily variations of direct, diffuse and global irradiances, total UV irradiance, downward LW irradiances, and aerosol optical depth versus water vapor content for the 7 selected days. There are two completely clear-sky (22 May and 17 June) and the other days are partly cloudy, which have relatively small aerosol loading. The maximum values of direct, global, and total UV irradiances are 1063 Wm^{-2} , 1011 Wm^{-2} , 50.4 Wm^{-2} under clear-sky condition, respectively, with corresponding value of 80 Wm^{-2} for diffuse irradiance. The downward LW irradiance with shadow is slightly smaller than that without shadow, both of which is corrected by case and dome temperature. Fig. 2(d) exhibits significant variations of AOD and columnar water vapor content for our cases.

3.2. Aerosol optical parameters

A comparison of AOD at 500 nm derived from CIMEL sun photometer and PREDE sky radiometer at Minqin is shown in Fig. 3. We also simulate the AOD_{500} using ratios of spectral direct and diffuse radiation as well as with solid view angle of sky radiometer. This method uses diffuse radiations measured within scattering angle range

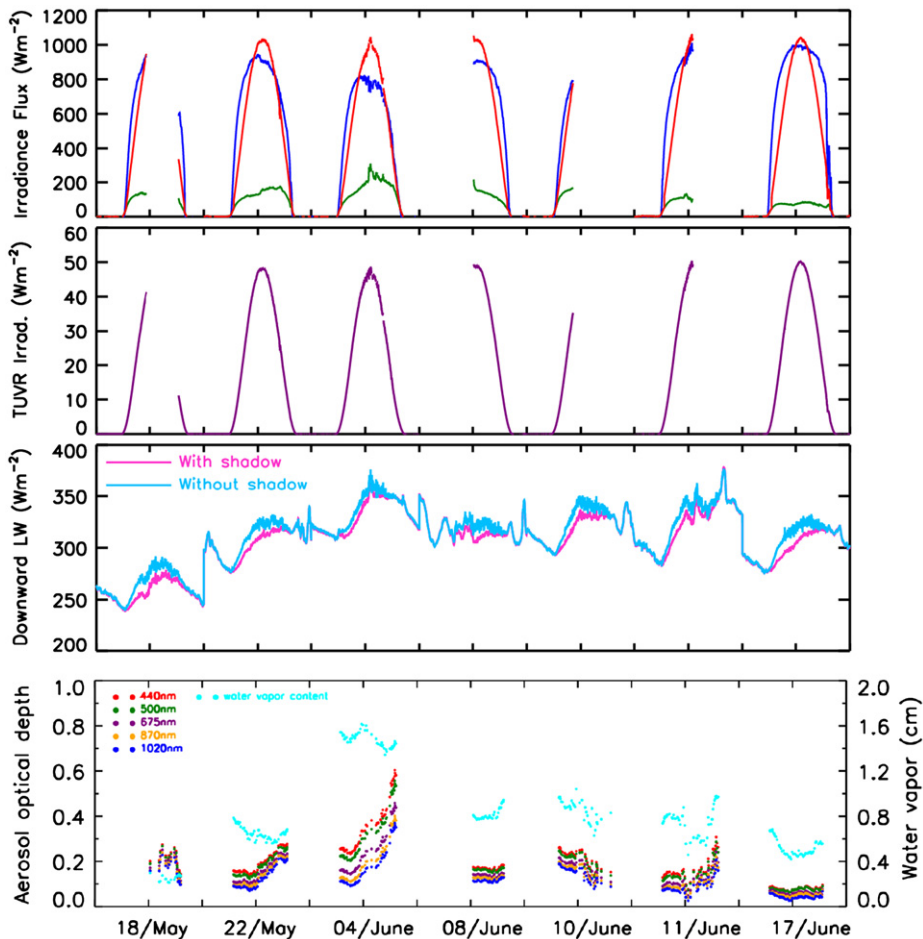


Fig. 2. Daily variations of ground-based measurements of (a) direct (red), diffuse (green) and global irradiances (blue), (b) total UV irradiance, (c) downward long wave irradiances with (pink) and without (deep sky blue) shadow, and (d) water vapor content (cyan), AOD at 440 nm (red), 500 nm (green), 675 nm (purple), 870 nm (orange), and 1020 nm (blue). (For interpretation of the references to color in this figure legend, the reader is referred to the web version of this article.)

of 3–30°. The detailed inversion algorithm is given by Nakajima et al. [23]. The simulated AOD₅₀₀ from sky radiometer is denoted as mean (POMRe) with green font in Fig. 3. The results retrieved from CIMEL sun photometer are comparable to the PREDE sky radiometer. The AOD₅₀₀ values range from 0.12 to 0.28 for May 22 and from 0.04 to 0.08 for June 17. The June 17 to some extent represents the background level of aerosol loading. From Fig. 3(a), we can see that the diurnal variation of AOD₅₀₀ is greatly consistent for the two instruments. And for May 22th case, the daily mean AOD₅₀₀ values of CIMEL and PREDE are 0.182 and 0.183, respectively. Fig. 4 presents an Ångström plot using log AOD versus log wavelength between CIMEL (red) and PREDE (blue) on May 22, 2010 at Minqin. It also reveals that the AOD in several wavelengths from CIMEL agrees well with the PREDE, with averaged Ångström exponent values of 0.462 and 0.514, respectively. It is noting that CIMEL possesses 440 nm wavelength but with 400 nm channel for PREDE. In spite of different observed protocols and the independent inversion algorithms, the two instruments exhibit virtually

the identical magnitude and wavelength dependence of AOD. As previously stated, the difference of AOD measured by CIMEL and PREDE can achieve within ± 0.02 during our IOP in 2010.

Fig. 5 illustrates the daily mean precipitable water (PW) derived from radiosonde and sun photometer during the intensive observations period (IOP). The radiosonde data (i.e., pressure, air temperature, and relative humidity profiles) is obtained from Minqin meteorology station (38.63°N, 103.08°E, 1367 m above MSL), which is about 10 km far away from Minqin site. During the intensive observations period, the radiosondes were launched 2 times each day and the integrated PW is derived by utilizing the equations by McCartney [25]. Halthore et al. [3] demonstrated that radiosonde measurements of precipitable water vapor agree to within ± 10% of microwave radiometer measurements made at the SGP/GART site during April 1996. Thus we designate an expected uncertainty of ± 10% PW for radiosonde data. Fig. 5 displays that the time series of daily mean PW from in situ radiosonde measurements is in accordance with the CIMEL sun

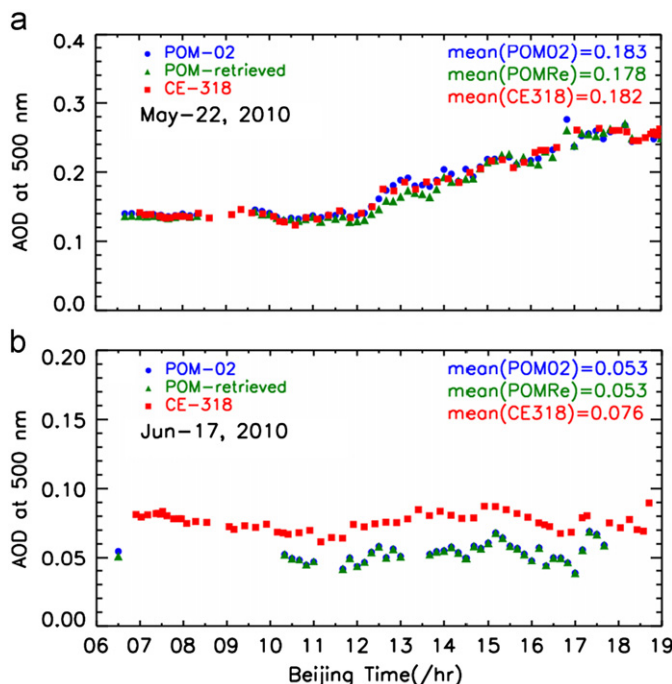


Fig. 3. Comparisons of AOD at 500 nm derived from CIMEL sun photometer and PREDE sky radiometer on (a) May 22, and (b) June 17, 2010 at Minqin site.

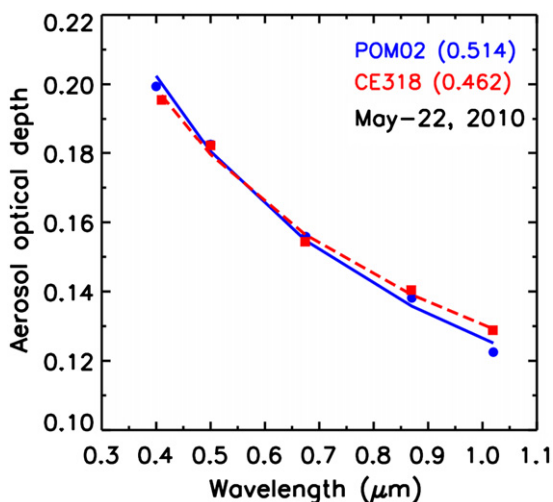


Fig. 4. Ångström exponent fits to AOD obtained by CIMEL sun photometer (red) and PREDE sky radiometer (blue) on May 22, 2010 at Minqin site. (For interpretation of the references to color in this figure legend, the reader is referred to the web version of this article.)

photometer. The overall averaged PW of radiosonde and CIMEL are 1.07 ± 0.36 and 1.02 ± 0.37 , respectively. Thereby, we conclude that the radiosonde measurements and sun photometer agree with each other within the expected observational uncertainty of PW.

Fig. 6 shows the time series of AOD_{500} , Ångström exponent $\alpha_{440,870}$, SSA_{675} , ASY_{675} , and columnar water vapor content for the 69 selected cases. These quantities

all exhibit large day-to-day variations although there are little dust storms observed during the measurements. Instead the atmospheric conditions are relatively clean with AOD_{500} all less than 0.5 during the entire period. It is noted that daily mean AOD_{500} presents a negative correlation with $\alpha_{440,870}$ (see Fig. 6a). It means that when the daily average AOD_{500} increases, the values of $\alpha_{440,870}$ decreases, and vice versa. This is expected because the larger AOD often corresponds to larger dust particles (i.e., smaller α). The value of AOD_{500} ranges from 0.06 to 0.50, and water vapor content varies within 0.24 to 1.53 cm range. The total average AOD_{500} and $\alpha_{440,870}$ are 0.18 ± 0.09 and 0.58 ± 0.22 respectively. The single-scattering albedo and asymmetry factor at 675 nm (i.e., SSA_{675} and ASY_{675}) range from 0.83 to 0.98 and from 0.65 to 0.76, corresponding to the mean values of 0.928 ± 0.035 , 0.712 ± 0.023 , respectively. Bi et al. [26] suggested that the seasonal mean SSA values of aerosol vary within 0.87–0.96 range over Loess Plateau in Northwestern China. Kim et al. [27] also presented that aerosols in East Asia have smaller SSAs (i.e., 0.89 for Asian dusts in Dunhuang, 0.9 for urban type aerosols in Yinchuan, and 0.88 for biomass burning aerosols in Sri-Samrong). All are close to our results. However, our analysis are much higher than that in Zhangye with 0.75 ± 0.02 at 500 nm [28] and over India with 0.74 to 0.84 of SSA_{500} [29].

3.3. Thermal dome offset correction

The thermal dome offset (also known as zero offset) is related to the heating difference between the instrument and its surroundings, which can lead to a measurement

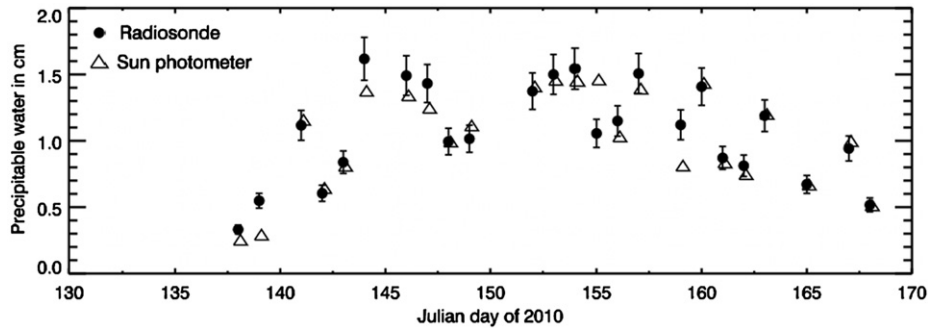


Fig. 5. Daily mean of precipitable water is derived from radiosonde and sun photometer during the IOP. The error bars of radiosonde values denote the expected uncertainty of PW for $\pm 10\%$.

uncertainty of exceeding 10 Wm^{-2} . World Meteorological Organization [30] pointed out that for any high-quality (or suitable for use as a working standard) pyranometer, this offset is currently tolerated to as large as 7 Wm^{-2} in response to 200 Wm^{-2} net thermal radiation under ventilated conditions, plus $\pm 2 \text{ Wm}^{-2}$ in response to a 5 K/h change in ambient temperature. In recent decades, numerous studies have focused on exploring the thermal offset problem of diffuse irradiance measurements and developed various algorithms to correct the observed data [31–34]. It is well known that PSP pyranometer and PIR pyrgeometer use the same case and thermopile sensor but with different types of dome. In this paper, we use a collocated thermopile pyrgeometer with a shadow and ventilator to correct the thermal dome offset of diffuse irradiance measurement. The corrected quantity is denoted as *corr*. According to Bush et al. [31], *corr* can be expressed as:

$$\text{corr} = K_0 + K_1 \times \text{NetIR} + K_2 \times \sigma \times [T_d^4 - T_c^4], \quad (1)$$

where *corr* is the corrected offset in Wm^{-2} , *NetIR* is the net IR irradiance measured by the thermopile of a shaded and ventilated pyrgeometer, σ is Stefan-Boltzmann constant, T_d and T_c are measured dome and case temperatures of pyrgeometer, and K_x is the regression coefficients. The corrected diffuse irradiance ($\text{Diff}_{\text{corr}}$) is then given by:

$$\text{Diff}_{\text{corr}} = \text{Diff}_0 - \text{corr}, \quad (2)$$

where Diff_0 is the uncorrected diffuse irradiance.

Note that *corr*, *NetIR*, T_d , and T_c can be recorded in 1-min interval. Nighttime data from 00:00 to 05:00 (local time) were used to generate the thermal offset corrections of the diffuse pyranometer through implementation of least squares fits to Eq. (1). Hence the corrected diffuse irradiance ($\text{Diff}_{\text{corr}}$) is determined from Eq. (2). Fig. 7 shows the corrected and uncorrected diffuse irradiances from a PSP pyranometer, and SBDART modeled Rayleigh diffuse irradiance on May 18, May 22, June 8, and June 17, 2010 at Minqin. It indicates that the corrected diffuse irradiances can compensate approximately $8\text{--}12 \text{ Wm}^{-2}$ under clear-sky and about $4\text{--}6 \text{ Wm}^{-2}$ under cloudy days in our cases. At the same time, the corrected data keeps at or above the results of Rayleigh simulations, even at large solar zenith angle.

4. Results and analysis

4.1. Radiative transfer calculations

To evaluate the solar irradiances we used the Santa Barbara Discrete-ordinate Atmospheric Radiative Transfer (SBDART, version 2.4) model, which is developed at University of California, Santa Barbara [35]. SBDART is a software tool that calculates plane-parallel radiative transfer under clear and cloudy conditions within the Earth's atmosphere and at the surface. All important processes that affect the ultraviolet, visible, and infrared radiation fields are included. This code uses a 2 to 8-stream discrete ordinate approximation and transmission function calculated by LOWTRAN, fit with a 3 term exponential sum. Previous works has verified that SBDART presented good agreement with other established radiative transfer models [13,36]. Halthore et al. [12] confirmed that the broadband spectrum irradiance estimated by SBDART agrees well with measurements (less than 3%). The aerosol optical depths, single-scattering albedo, asymmetry factor and their wavelength dependence of spectral variations, column precipitable water vapor, total ozone amounts, and spectral surface albedo are the main input parameters to run the model. In this study, aerosol optical properties, such as AOD, SSA, ASY at 440, 675, 870 and 1020 nm wavelengths along with Ångström exponent are retrieved from CIMEL sun photometer [20]. The Ångström formula is employed to extrapolate AODs beyond measured wavelengths. SSAs and ASYs at other wavelengths are interpolated and extrapolated from combining the observations and continental polluted model of optical of aerosols and clouds (OPAC) [37]. The temperature, pressure, and relative humidity vertical profiles up to about 12 km height for the calculations have been measured from radiosonde data, launching at the nearby location. Above this altitude the standard mid-latitude summer atmospheric profiles were filled up. In this article, we used the daily mean radiosonde profiles in SBDART. Daily total ozone amount is obtained from the Ozone Monitoring Instrument (OMI, NASA Aura mission), ranging from 314 DU to 355 DU in our cases. The spectrally dependent surface reflectance at Minqin is inferred from the 500 m resolution Moderate Resolution Imaging Spectroradiometer (MODIS)

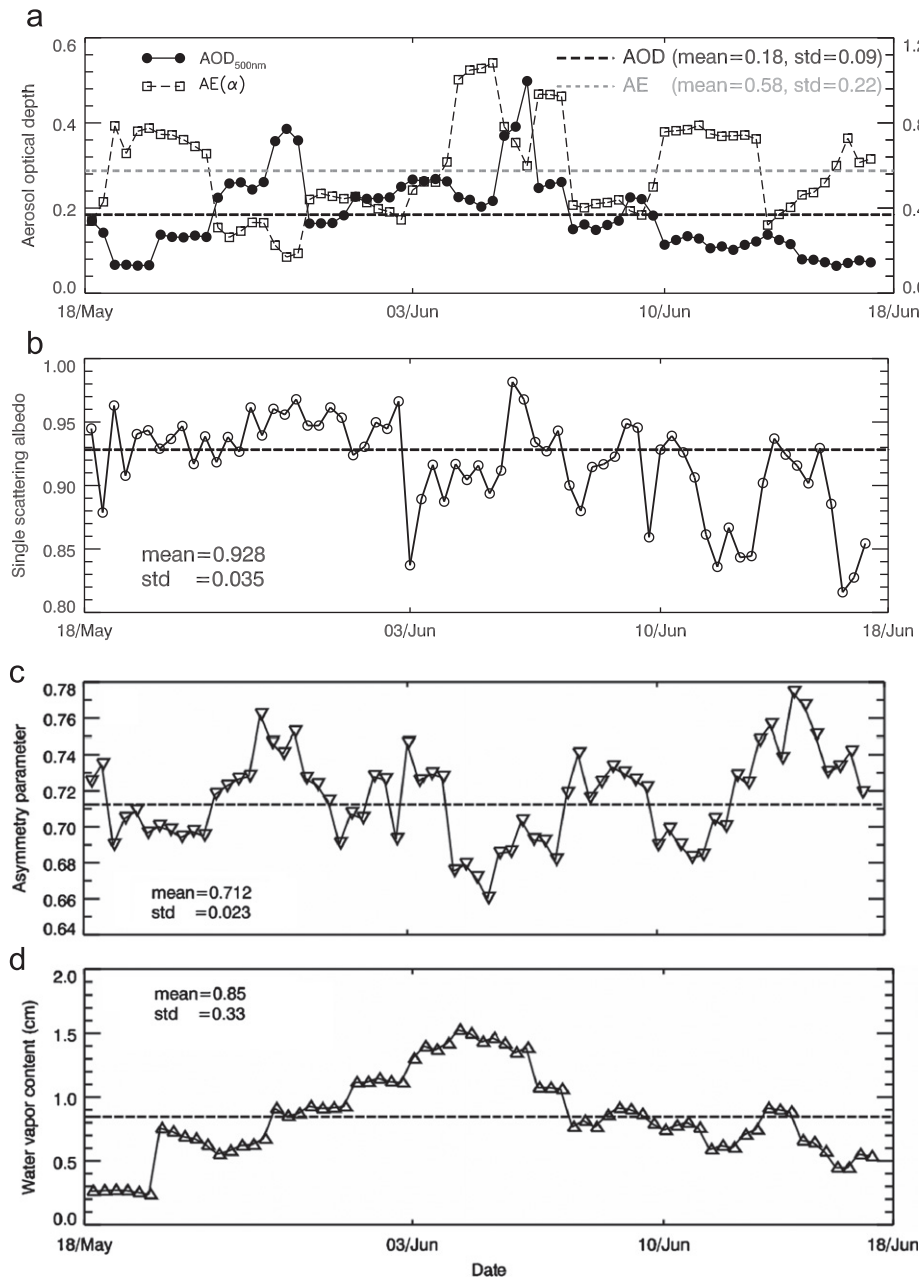


Fig. 6. Time series of (a) aerosol optical depth (AOD) at 500 nm and Ångström exponent (440–870 nm), (b) single-scattering albedo, (c) asymmetry factor at 675 nm, and (d) columnar water vapor content in cm for the 69 cases.

bidirectional reflectance distribution function/Albedo products [38]. MODIS can provide both black-sky albedo (BSA)-direct reflectance and white-sky albedo (WSA)-bihemispherical reflectance at seven spectral bands (0.47, 0.555, 0.659, 0.858, 1.24, 1.64, and 2.10 μm) as well as three broad bands (0.4–0.7, 0.7–3.0, and 0.4–3.0 μm). Finally, we determined the fractions of soil and vegetation are 90% and 10%, respectively. Surface solar radiative fluxes from 0.285 to 2.80 μm spectral wavelength were computed through application of the SBDART.

4.2. Comparison between simulations and measurements

Fig. 8 presents the comparisons of SBDART model simulated and ground-based measured values of surface irradiances at Minqin. We calculate the global solar irradiance as the sum of direct solar radiation multiplied by the cosine of solar zenith angle plus diffuse irradiance. And the total solar irradiance directly from PSP pyranometer is also used in the comparison (Fig. 8d) although there may be more uncertainty when the solar zenith

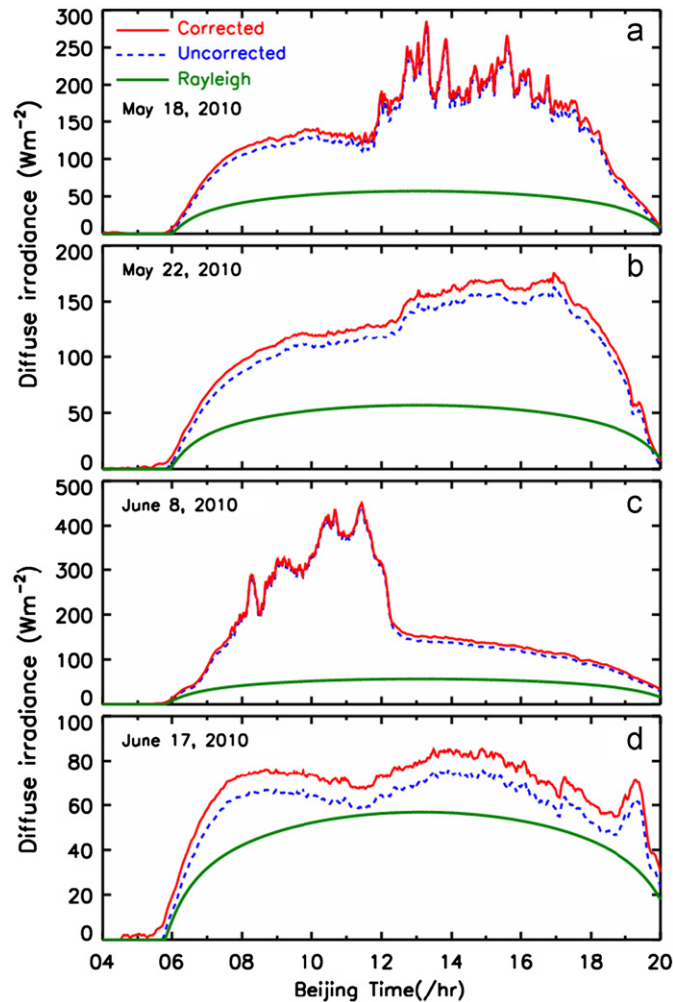


Fig. 7. Corrected (red) and uncorrected (blue) diffuse irradiances from a PSP pyranometer, and the modeled Raleigh diffuse irradiance on (a) May 18, (b) May 22, (c) June 8, and (d) June 17, 2010 at Minqin site. (For interpretation of the references to color in this figure legend, the reader is referred to the web version of this article.)

angle is high due to different responses of detector at high solar incident angle [39]. Our results exhibit excellent agreements for radiative quantities. In general, the good agreement of direct irradiance indicates that the input values of AOD and gas absorption are accurate, both in magnitude and spectral dependence. There are a few divergent points for diffuse fluxes that are often related to the retrieved high values of SSA and ASY. But most of the good agreements for diffuse irradiances also indicate that, to some extent, the retrieved SSA and ASY are reliable. The correlation coefficients range from 0.985 to 0.999. Fig. 8c and d, show that the agreement between the model and observation for the global irradiances is better for the summation than the direct measurements.

The differences between simulations and measurements are displayed in Fig. 9. The absolute difference of (model–measurement) ranges from -38 Wm^{-2} to $+10.7 \text{ Wm}^{-2}$ for the direct irradiance, from -8.7 to $+20 \text{ Wm}^{-2}$ for diffuse irradiance, and from -32 to $+18.6 \text{ Wm}^{-2}$ for global irradiance. The corresponding

percent differences are: -11.1% to $+3.1\%$, -7.9% to 17.7% , and -7.0% to 4.1% , respectively. The mean differences (MED, designated as mean simulation minus mean observation) are -9.1 Wm^{-2} (-2.6%) for the direct irradiance, $+3.1 \text{ Wm}^{-2}$ ($+2.8\%$) for diffuse irradiance, and -6.0 Wm^{-2} (-1.3%) for global irradiance, with corresponding standard deviations of 12.1 Wm^{-2} , 6.8 Wm^{-2} , and 12.1 Wm^{-2} , respectively. Wang et al. [14] performed sensitivity experiments and found that decreasing AOD by 0.02 would increase the direct normal irradiance from 20 to 40 Wm^{-2} . Kato et al. [40] showed that increasing the water vapor amount from 0.23 g/cm^2 to 0.86 g/cm^2 would reduce the direct normal irradiance by 42 Wm^{-2} . Hence, our simulation of direct irradiance is smaller than measurement, which may be partly attributed to overestimated AOD or overestimated WVC. The simulation of downward diffuse irradiance is slightly greater than measurements. However, this discrepancy is well within instrumental and model's uncertainties and is similar to previous results [5,12].

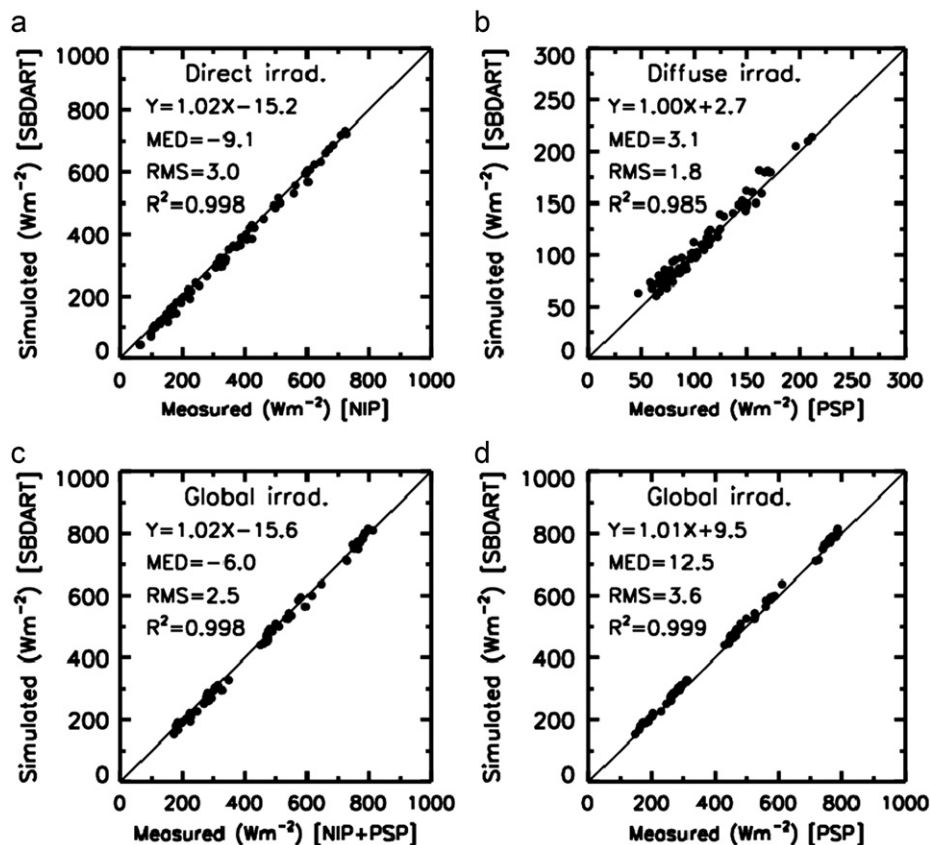


Fig. 8. Comparisons between the SBDART simulated and ground-based measured (a) direct, (b) diffuse, (c) global total from the sum of direct and diffuse irradiances, and (d) directly global irradiances from the unshaded pyranometer for the 69 cases. The 1:1 line (solid) is shown for comparison.

4.3. Aerosol direct radiative effect

4.3.1. Aerosol direct radiative forcing

Aerosol direct radiative forcing (ARF) is determined by means of computing the difference between net short-wave radiative fluxes with and without aerosols under cloudless conditions. Detailed approach is given by recent papers [41]. There are generally two independent methods to derive ARF [42]. The first method relies only on the direct ground-based or spaceborne observations to derive this quantity. The second method employs a combination of model and measurements. And we use the latter method in current study. The ARF at the surface depends strongly on aerosol loading and optical properties (e.g., SSA and ASY). We first compute the instantaneous ARF in 30 min interval utilizing the aforementioned method. For determining the daily averaged ARF, we postulate that the aerosol concentration remains relatively constant during the entire day and interpolated AOD and optical properties measurements across periods of cloud present and missing data (including nighttime) to create a continuous time series.

Fig. 10 shows the 24-h averaged ARF values at the top of the atmosphere (TOA), surface, and in the atmosphere for 7 selected days. The ARF values in the atmosphere are calculated from ARF at TOA minus those at surface. As is presented in Fig. 10, the daily mean ARFs are moderately

negative at the surface (-5.2 to -15.6 Wm^{-2}) and positive in the atmosphere (5.2 to 10.8 Wm^{-2}), which represents a cooling at the surface and slight warming in the atmosphere. The dust ARF at surface estimated in a semi-desert area of Northwestern China ranges from -7.9 to -35.8 Wm^{-2} [28] and -13 to -43 Wm^{-2} at three sites in East Asia [27], which are much larger than our values. High ARF values at the surface correspond to large aerosol loading or high AOD values. For instance, the maximum values of -15.6 Wm^{-2} for ARF at surface appears on June 04, coinciding with the high AOD_{500} value of 0.30. And daily mean ARFs at TOA vary within -4.8 to $+0.40 \text{ Wm}^{-2}$ range. Standard deviations commonly increase with the mean values of ARF.

Ge et al. [28] revealed that the anthropogenic aerosol has smaller AOD but stronger absorption (i.e., smaller SSA values) in a semi-desert area of Northwestern China during the spring of 2008 China–US joint field experiment. They also indicated that the dust ARF at TOA is neutral (less than 4 Wm^{-2}) and the corresponding values primarily depend on SSA value. Furthermore, similar results suggested that moderately strong absorptive aerosols were found in the north [43], south [44], and across China [45]. Overall, the global average ARF at TOA is generally estimated to be negative [46–47], which represents a cooling effect of aerosol on climatic system. On a regional scale, our results show that a slight cooling effect

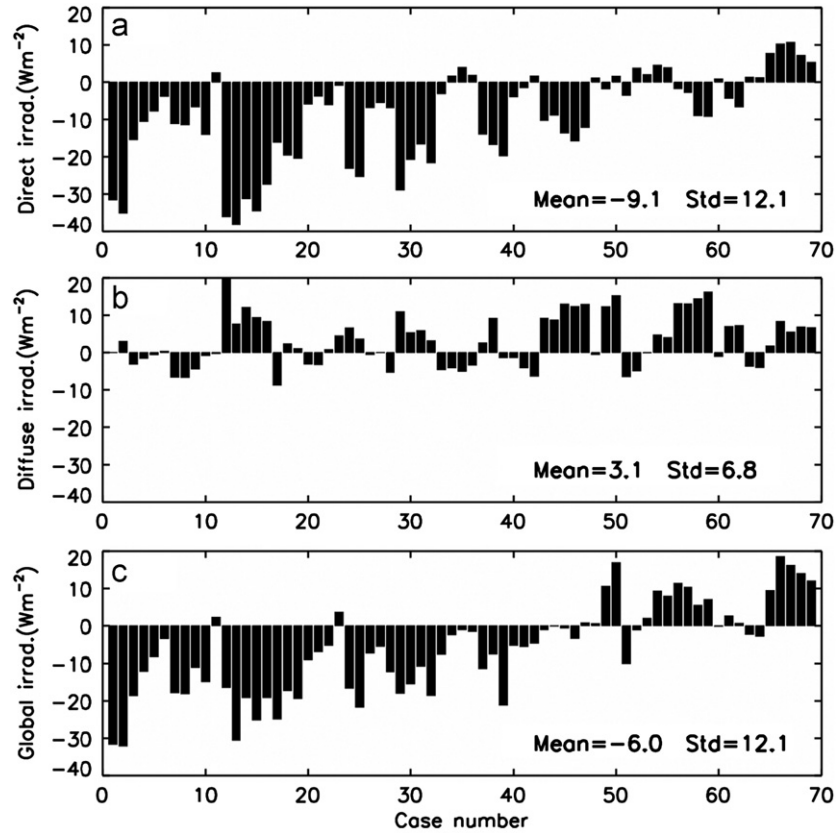


Fig. 9. Differences between the SBDART simulation and ground-based measurements of (a) direct, (b) diffuse, and (c) global irradiances for the 69 cases.

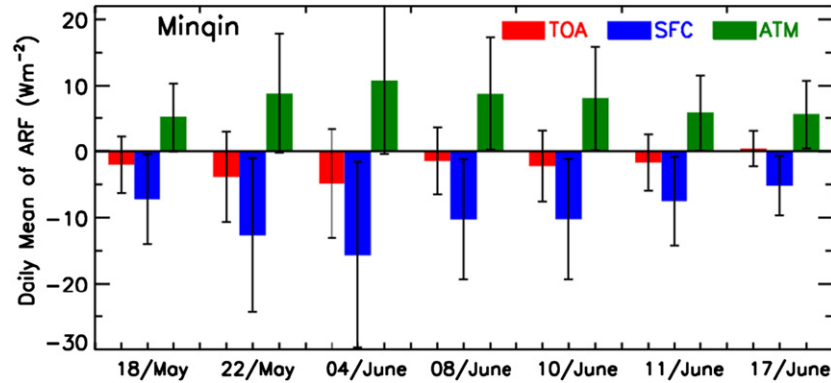


Fig. 10. Daily average values of aerosol direct radiative forcing at the surface (blue bars), TOA (red bars), and in the atmosphere (green bars) for seven clear-sky days (the bars indicate plus or minus one standard deviation). (For interpretation of the references to color in this figure legend, the reader is referred to the web version of this article.)

of aerosol under cloudless condition in Badain Jaran Desert area of Northwestern China.

4.3.2. Heating rate

The rate of atmospheric temperature changes ($\partial T/\partial t$) in a certain layer due to aerosol absorbed solar radiation can be expressed as:

$$\frac{\partial T}{\partial t} = -\frac{1}{\rho C_p} \frac{\Delta F}{\Delta Z} = \frac{g}{C_p} \Delta \frac{\Delta F}{\Delta P} \quad (3)$$

where ρ is the density of air and C_p is the specific heat capacity of the air at constant pressure, $(\Delta F/\Delta Z)$ is the radiative flux divergence. g is the acceleration of gravity, ΔF is the aerosol absorbed solar energy, and ΔP is the atmospheric pressure difference between the surface and the tropopause. ΔF is calculated as the differences in atmospheric absorbed solar radiation with and without aerosols.

Table 2 shows that heating rates in the whole atmosphere layer due to aerosols are 0.07, 0.11, 0.14, 0.11, 0.10,

Table 224-h average of AOD₅₀₀, ARFs in the atmosphere and aerosol radiative heating rates for the entire atmosphere for 7 selected cloudless days.

	May 18	May 22	June 04	June 08	June 10	June 11	June 17
AOD ₅₀₀	0.156	0.191	0.303	0.158	0.209	0.125	0.079
ARF _{SFC} (Wm ⁻²)	5.17	8.81	10.78	8.78	8.00	5.82	5.58
Heating rate (K/day)	0.066	0.113	0.138	0.112	0.102	0.075	0.072

0.08, and 0.07 K/day for 7 selected cloudless days. These values may represent the heating rates due to background aerosols. It is distinct that high heating rates correspond with high AOD and high ARF in the atmosphere. Liu et al. [48] suggested that the maximum daily average of heating rate could reach 2 K/day for strong dusty day and within about 1.25 K/day under background aerosols over the Loess Plateau in Northwestern China. Huang et al. [43,49] studied the dust aerosol vertical distributions and heating rate over Taklimakan Desert using the Fu–Liou radiative transfer model along with satellite observations. They reported that the dust aerosols heat the atmosphere (daily mean) by up to 1, 2, and 3 K/day for light, moderate, and heavy dust layers, respectively. Obviously, former outcome of dust aerosols in Northwestern China are about 10 times more than our cloudless cases. This is partly because we reported the mean aerosol radiative heating rate for the entire atmosphere while previous studies often reported the aerosol radiative heating rates at the aerosol layers. Several studies have shown that the atmospheric heating by absorbing particles may evaporate low-level clouds, resulting in a decrease of cloud cover and planetary albedo [50–51]. Huang et al. [43,52–55] also suggested that higher dust aerosol heating rates due to enhanced atmospheric absorption over Taklimakan desert in Northwestern China can have an impact on regional climate and monsoon circulation. Therefore, a detailed and thorough investigation on the impacts of enhanced aerosol heating under large aerosol loading conditions in Northwestern China and their effect on regional climate warrants further studies.

5. Conclusions and remarks

The primary objective of this article was to compare the simulated and measured clear-sky solar irradiances and examine the corresponding aerosol direct radiative forcing and heating rate in Badain Jaran Desert of Northwestern China, during the intensive field experiment in spring of 2010 (April–June). Based on the high-precision ground-based radiation measurements, AERONET products, we computed the direct, diffuse, and global irradiances using SBDART radiative transfer model. The key input parameters for the radiative transfer models include aerosol optical depths, single-scattering albedo, asymmetry factor and their wavelength dependence, column precipitable water vapor, total ozone amounts, and spectral surface albedo. The mean differences between model and measurements are -9.1 Wm^{-2} (-2.6%) for the direct irradiance, $+3.1 \text{ Wm}^{-2}$ ($+2.8\%$) for diffuse irradiance, and -6.0 Wm^{-2} (-1.3%) for global irradiance, which shows an excellent radiative closure.

Aerosol shortwave direct radiative forcing is estimated at the TOA, surface, and in the atmosphere. The daily mean ARF are moderately negative values at the surface (-5.2 to -15.6 Wm^{-2}) and positive values in the atmosphere (5.2 to 10.8 Wm^{-2}), which represents a cooling at the surface and slight warming in the atmosphere.

The positive values of ARF in the atmosphere represent that aerosol particles possibly absorb the solar radiation and heat the atmospheric layer. The daily mean of heating rates in the whole atmosphere layer are 0.07, 0.11, 0.14, 0.11, 0.10, 0.08, and 0.07 K/day for 7 selected cloudless days. Our results are about 10 times smaller than recent studies of dust aerosols over Loess Plateau (1.25 K/day) and Taklimakan Desert (1 K/day) in Northwestern China which are for the heating in the dust layers.

In this paper, we only examined 7 selected cloudless days with background aerosol loading. In order to improve the accuracy of model simulations and advance our understanding of aerosol radiative effect, especially for heating rate, further effort should be dedicated to validating more cases under high aerosol optical depth days and different regions in Northwestern China.

Acknowledgments

SACOL was sponsored by Lanzhou University through 985 Program. This work was jointly supported by the National Basic Research Program of China (2012CB955302) and National Science Foundation of China under grant 41175134 and 41105019. The Fundamental Research Funds for the Central Universities lzujbky-2010-k06, and the Developmental Program of Changjiang Scholarship and Innovative Research Team (IRT1018). We are grateful to Prof. Nakajima for supplying SKYRAD software. AERONET/BRDF/TOMS/CERES data supplied by NASA are greatly appreciated. We would also like to thank all anonymous reviewers for their constructive and insightful comments.

References

- [1] Liou KN. An introduction to atmospheric radiation. second edition. New York: Elsevier Academic Press; 2002. 583 pp.
- [2] Fu Q, Cribb MC, Barker HW, Krueger SK, Grossman A. Cloud geometry effects on atmospheric solar absorption. *J Atmos Sci* 2000;57:1156–68.
- [3] Halthore RN, Schwartz SE, Michalsky JJ, Anderson GP, Ferrare RA, Holben BN, Ten Brink HM. Comparison of model estimated and measured direct-normal solar irradiance. *J Geophys Res* 1997;102:29991–30002, <http://dx.doi.org/10.1029/97JD02628>.
- [4] Kato S, Ackerman TP, Clothiaux EE, Mather JH, Mace GG, Wesely ML, Murcray F, Michalsky J. Uncertainties in modeled and measured clear-sky surface shortwave irradiances. *J Geophys Res* 1997;102:25881–98, <http://dx.doi.org/10.1029/97JD01841>.

- [5] Ge J, Huang J, Su J, Bi J, Fu Q. Shortwave radiative closure experiment and direct forcing of dust aerosol over northwestern China. *Geophys Res Lett* 2011;38:L24803, <http://dx.doi.org/10.1029/2011GL049571>.
- [6] Fu Q, Lesins G, Higgins J, Charlock T, Chylek P, Michalsky J. Broadband water vapor absorption of solar radiation tested using ARM data. *Geophys Res Lett* 1998;25:1169–72.
- [7] Halthore RN, Nemesure S, Schwartz SE, Emre DG, Berk A, Dutton EG, Bergin MH. Models overestimate diffuse clear-sky irradiance: a case for excess atmospheric absorption. *Geophys Res Lett* 1998;25:3591–4.
- [8] Henzing JS, Knap WH, Stammes P, Apituley A, Bergwerff JB, Swart DPJ, Kos GPA, ten Brink HM. Effect of aerosols on the downward shortwave irradiances at the surface: Measurements versus calculations with MODTRAN4.1. *J Geophys Res* 2004;109:D14204, <http://dx.doi.org/10.1029/2003JD004142>.
- [9] Philipona R. Underestimation of solar global and diffuse radiation measured at Earth's surface. *J Geophys Res* 2002;107(D22):4654, <http://dx.doi.org/10.1029/2002JD002396>.
- [10] Halthore RN, Schwartz SE. Comparison of model estimated and measured diffuse downward irradiance at surface in cloud-free skies. *J Geophys Res* 2000;105(D15):20165–77, <http://dx.doi.org/10.1029/2000JD900224>.
- [11] Powell DM, Kato S, Haeffelin M, Dubovik O. Clear-sky model and measurement comparison from the first diffuse irradiance IOP—fall. In: *Proceeding of the Twelfth ARM Science Team*. St. Petersburg, Florida; April 8–13 2002.
- [12] Halthore RN, et al. Intercomparison of shortwave radiative transfer codes and measurements. *J Geophys Res* 2005;110:D11206, <http://dx.doi.org/10.1029/2004JD005293>.
- [13] Michalsky JJ, Anderson GP, Barnard J, Delamere J, Gueymard C, Kato S, Kiedron P, McComiskey A, Ricchizzi P. Shortwave radiative closure studies for clear skies during the Atmospheric Radiation Measurement 2003 Aerosol Intensive Observation Period. *J Geophys Res* 2006;111:D14S90, <http://dx.doi.org/10.1029/2005JD006341>.
- [14] Wang P, Knap WH, Kuipers Munneke P, Stammes P. Clear-sky shortwave radiative closure for the Cabauw Baseline Surface Radiation Network site, Netherlands. *J Geophys Res* 2009;114:D14206, <http://dx.doi.org/10.1029/2009JD011978>.
- [15] Huang JP, Zhang W, Zuo JQ, Bi JR, Shi JS, Wang X, Chang ZL, et al. An overview of the semi-arid climate and environment research observatory over the Loess Plateau. *Adv Atmos Sci* 2008;25(6):906–21, <http://dx.doi.org/10.1007/s00376-008-0906-7>.
- [16] Zhou ZJ. Blowing-sand and sandstorm in China in recent 45 years. *Quaternary Sciences* 2001;21(1):9–17 [in Chinese].
- [17] Holben BN, Eck TF, Slutsker I, et al. AERONET-A federated instrument network and data archive for aerosol characterization. *Remote Sensing Environ* 1998;66(1):1–16, [http://dx.doi.org/10.1016/S0034-4257\(98\)00031-5](http://dx.doi.org/10.1016/S0034-4257(98)00031-5).
- [18] Eck TF, Holben BN, Reid JS, Dubovik O, Smirnov A, O'Neill NT, Slutsker I, Kinne S. Wavelength dependence of the optical depth of biomass burning, urban and desert dust aerosols. *J Geophys Res* 1999;104:31333–50.
- [19] Schmid B, Michalsky JJ, Slater DW, Barnard JC, Halthore RN, Liljegren JC, Holben BN, Eck TF, Livingston JM, Russell PB, Ingold T, Slutsker I. Comparison of columnar water vapor measurements from solar transmittance methods. *Appl Opt* 2001;40(12):1886–96.
- [20] Dubovik O, King MD. A flexible inversion algorithm for the retrieval of aerosol optical properties from Sun and sky radiance measurements. *J Geophys Res* 2000;105(D16):20673–96.
- [21] Smirnov A, Holben BN, Eck TF, Dubovik O, Slutsker I. Cloud screening and quality control algorithms for the AERONET data base. *Remote Sens Environ* 2000;73(3):337–49.
- [22] Takamura T, Takenaka H, Cui Y, Nakajima Takashi Y, Higurashi A, Fukuda S, Kikuchi N, Nakajima T, Sano I, Pinker Rachel T. Aerosol and cloud validation system based on SKYNET observations: Estimation of shortwave radiation budget using ADEOS-II/GLI data. *J Remote Sens Soc Jpn* 2009;29(1):40–53.
- [23] Nakajima T, Tonna G, Rao R, Boi P, Kaufman Y, Holben B. Use of sky brightness measurements from ground for remote sensing of particulate polydispersions. *Appl Opt* 1996;35(15):2672–86.
- [24] Ohmura A, et al. Baseline surface radiation network (BSRN/WCRP): New precision radiometry for climate research. *Bull Am Meteorol Soc* 1998;79:2115–36.
- [25] McCartney EJ. *Optics of the atmosphere*. New York: John Wiley; 1976. 408 pp.
- [26] Bi J, Huang J, Fu Q, Wang X, Shi J, Zhang W, Huang Z, Zhang B. Toward characterization of the aerosol optical properties over Loess Plateau of Northwestern China. *J Quant Spectrosc Radiat Transfer* 2011;112:346–60, <http://dx.doi.org/10.1016/j.jqsrt.2010.09.006>.
- [27] Kim D-H, Sohn BJ, Nakajima T, Takamura T. Aerosol radiative forcing over East Asia determined from ground-based solar radiation measurements. *J Geophys Res* 2005;110:D10S22, <http://dx.doi.org/10.1029/2004JD004678>.
- [28] Ge J, Su J, Ackerman TP, Fu Q, Huang J, Shi J. Dust aerosol optical properties retrieval and radiative forcing over northwestern China during the 2008 China–US joint field experiment. *J Geophys Res* 2010;115:D00K12, <http://dx.doi.org/10.1029/2009JD013263>, [printed 116(D7), 2011].
- [29] Pandithurai G, Dipu S, Dani KK, Tiwari S, Bisht DS, Devara PCS, Pinker RT. Aerosol radiative forcing during dust events over New Delhi, India. *J Geophys Res* 2008;113:D13209, <http://dx.doi.org/10.1029/2008JD009804>.
- [30] World Meteorological Organization. *Guide to meteorological instruments and methods of observation*. 7th ed., WMO-8. Geneva, Switzerland; 2008.
- [31] Bush BC, Valero FPJ, Simpson AS, Bignone L. Characterization of thermal effects in pyranometers: a data correction algorithm for improved measurement of surface insolation. *J Atmos Oceanic Technol* 2000;17:165–75.
- [32] Haeffelin M, Kato S, Smith AM, Rutledge K, Charlock T, Mahan JR. Determination of the thermal offset of the Eppley Precision Spectral Pyranometer. *Appl Opt* 2001;40:472–84, <http://dx.doi.org/10.1364/AO.40.000472>.
- [33] Dutton EG, Michalsky JJ, Stoffel T, Forgan BW, Hickey J, Nelson DW, Alberta TL, Reda I. Measurement of broadband diffuse solar irradiance using current commercial instrumentation with a correction for thermal offset errors. *J Atmos Oceanic Technol* 2001;18:297–314.
- [34] Ji Q, Tsay S-C. A novel nonintrusive method to resolve the thermal dome effect of pyranometers: Instrumentation and observational basis. *J Geophys Res* 2010;115:D00K21, <http://dx.doi.org/10.1029/2009JD013483>, [printed 116(D7), 2011].
- [35] Ricchiazzi P, Yang S, Gautier C, Sowle D. SBDART: a research and teaching software tool for plane-parallel radiative transfer in the Earth's atmosphere. *Bull Am Meteorol Soc* 1998;79:2101–14, [http://dx.doi.org/10.1175/1520-0477\(1998\)079<2101:SARATS>2.0.CO;2](http://dx.doi.org/10.1175/1520-0477(1998)079<2101:SARATS>2.0.CO;2).
- [36] Ackerman TP, Flynn DM, Marchand RT. Quantifying the magnitude of anomalous solar absorption. *J Geophys Res* 2003;108:4273, <http://dx.doi.org/10.1029/2002JD002674>.
- [37] Hess M, Koepke P, Schult I. Optical properties of aerosols and clouds: The software package OPAC. *Bull Am Meteorol Soc* 1998;79:831–44.
- [38] Moody EG, King MD, Platnick S, Schaaf CB, Gao F. Spatially complete global spectral surface albedos: value-added datasets derived from Terra MODIS land products. *IEEE Trans Geosci Remote Sens* 2005;43:144–58, <http://dx.doi.org/10.1109/TGRS.2004.838359>.
- [39] Michalsky JJ, Harrison LC, Berkheiser III WE. Cosine response characteristics of some radiometric and photometric sensors. *Sol Energy* 1995;54:397–402.
- [40] Kato S, Ackerman TP, Dutton EG, Laulainen N, Larson N. A comparison of modeled and measured surface shortwave irradiance for a molecular atmosphere. *J Quant Spectrosc Radiat Transfer* 1999;61(4):493–502.
- [41] Su J, Huang J, Fu Q, Minnis P, Ge J, Bi J. Estimation of Asian dust aerosol effect on cloud radiation forcing using Fu–Liou radiative model and CERES measurements. *Atmos Chem Phys* 2008;8:2763–71.
- [42] Satheesh SK, Ramanathan V. Large differences in tropical aerosol forcing at the top of atmosphere and Earth's surface. *Nature* 2000;405:60–3.
- [43] Huang J, Fu Q, Su J, Tang Q, Minnis P, Hu Y, Yi Y, Zhao Q. Taklimakan dust aerosol radiative heating derived from CALIPSO observations using the Fu–Liou radiation model with CERES constraints. *Atmos Chem Phys* 2009;9:4011–21.
- [44] Xia X, Li Z, Holben B, Wang P, Eck T, Chen H, Cribb M, Zhao Y. Aerosol optical properties and radiative effects in the Yangtze Delta region of China. *J Geophys Res* 2007;112:D22S12, <http://dx.doi.org/10.1029/2007JD008859>.
- [45] Li Z, Lee K-H, Wang Y, Xin J, Hao W-M. First observation-based estimates of cloud-free aerosol radiative forcing across China. *J Geophys Res* 2010;115:D00K18, <http://dx.doi.org/10.1029/2009JD013306>, [printed 116(D7), 2011].

- [46] Kim D-H, Ramanathan V. Solar radiation budget and radiative forcing due to aerosols and clouds. *J Geophys Res* 2008;113: D02203, <http://dx.doi.org/10.1029/2007JD008434>.
- [47] Yu H, et al. A review of measurement-based assessments of the aerosol direct radiative effect and forcing. *Atmos Chem Phys* 2006;6:613–66, <http://dx.doi.org/10.5194/acp-6-613-2006>.
- [48] Liu Y, Huang J, Shi G, Takamura T, Khatri P, Bi J, Shi J, Wang T, Wang X, Zhang B. Aerosol optical properties and radiative effect determined from sky-radiometer over Loess Plateau of Northwest China. *Atmos Chem Phys* 2011;11:11455–63.
- [49] Huang J, Minnis P, Yi Y, Tang Q, Wang X, Hu Y, Liu Z, Ayers K, Trepte C, Winker D. Summer dust aerosols detected from CALIPSO over the Tibetan Plateau. *Geophys Res Lett* 2007;34:L18805, <http://dx.doi.org/10.1029/2007GL029938>.
- [50] Ackerman AS, Toon OB, Stevens DE, Heymsfield AJ, Ramanathan V, Welton EJ. Reduction of tropical cloudiness by soot. *Science* 2000;288:1042–7, <http://dx.doi.org/10.1126/science.288.5468.1042>.
- [51] Hansen J, Sato M, Ruedy R. Radiative forcing and climate response. *J Geophys Res* 1997;102:6831–64, <http://dx.doi.org/10.1029/96JD03436>.
- [52] Huang J, Minnis P, Lin B, Wang T, Yi Y, Hu Y, Sun-Mack S, Ayers K. Possible influences of Asian dust aerosols on cloud properties and radiative forcing observed from MODIS and CERES. *Geophys Res Lett* 2006;33:L06824, <http://dx.doi.org/10.1029/2005GL024724>.
- [53] Huang J, Lin B, Minnis P, Wang T, Wang X, Hu Y, Yi Y, Ayers JR. Satellite-based assessment of possible dust aerosols semi-direct effect on cloud water path over East Asia. *Geophys Res Lett* 2006;33, <http://dx.doi.org/10.1029/2006GL026561>.
- [54] Huang J, Wang Y, Wang T, Yi Y. Dusty cloud radiative forcing derived from satellite data for middle latitude regions of East Asia. *Prog Nat Sci* 2006;16(10):1084–9.
- [55] Huang J, Minnis P, Yan H, Yi Y, Chen B, Zhang L, Ayers JK. Dust aerosol effect on semi-arid climate over Northwest China detected from A-Train satellite measurements. *Atmos Chem Phys* 2010;10: 12465–95.